Methods

I. Experimental Set-up

CEP-stable < 6 fs laser pulses (Energy = 2.5 nJ) coming from our laser source were focused by a 25 cm long biconvex lens onto an Acousto-Optic-Frequency-Shifter (AOFS) at Bragg angle for maximum 1^{st} order diffraction efficiency. An amplified electromagnetic wave from a RF waveform generator at a slightly higher frequency than the repetition rate (f_r = 80 MHz) of the laser drives the AOFS ($f_r + f_0$ = 80 MHz + 0.8 kHz). The first order beam out of the AOFS will be frequency upshifted by the driving frequency of the AOFS, whereas the 0^{th} order beam will remain unaffected. An ultrashort CEP stable laser pulse comprises of an offset free frequency comb, whose n^{th} comb line is the n^{th} multiple of the repetition rate, nf_r. Thus, after the 1^{st} order diffraction, the n^{th} comb line after interaction with the AOFS is given as $(n+1)f_r + f_0$, while the 0^{th} order beam is nf_r. A small part of the beam after the AOFS (~ 1%) is guided to an interferometric set-up for measurement of the offset frequency between the 1^{st} and 0^{th} order diffraction beams. During the interferometric beating, the n^{th} comb line of the 1^{st} order diffracted beam will beat with the $(n+1)^{th}$ comb line of the 0^{th} order diffracted beam. The detected beat signal is used as a reference for the lock-in detection of the laser-induced tunneling current at the STM junction.

Most part of the beam after the AOFS (~ 99 %) is guided to a Michelson interferometer, where a half-wave plate in both arms of the interferometer rotates the polarization of the pulses in such a way that they are orthogonal to each other. The angle of the polarization axes with respect to the axis of the nanotip of the STM is 45º for both pulses, as shown in the extreme right corner in Fig. S1.

Multiple reflections off two sets of chirped dielectric mirrors with different group delay dispersion (GDD = -60 fs^2 and GDD = -120 fs^2) were used to compensate for the positive chirp that the ultrashort pulses acquire after passing through two lenses and the AOFS crystal. The pulse duration in both the interferometric arms is ~ 6 fs after the pulse compression stage. The temporal profiles of the laser pulses were measured with an interferometric nonlinear autocorrelator. Laser pulses after the Michelson-interferometer pass through an ultrathin fused silica window (thickness ~ 500 μm) before being focused by an off-axis parabolic mirror to the apex of the nanotip in the STM junction. The energy of the pulses used at the STM junction is ~ 150 pJ.

Long-term stability of the delay arm of the Michelson interferometer was verified by continuously measuring the nonlinear cross-correlation of the laser-induced tunneling current at the STM junction over several hours. Fig. S2 shows a series of nonlinear cross-correlation traces acquired over 30 minutes. The zero-overlap position of the Michelson interferometer changes negligibly (< 100 as) over several hours.

The custom-built STM operates in ultra-high vacuum conditions, P ~ 5 × 10^{-10} mbar, and at liquid nitrogen temperature (~ 80 K). The surface of the Au (111) crystal is prepared by sputtering cycles with 1.5 keV Ar+ ions followed by thermal annealing at 500 K. The PTCDA molecules were sublimated from a resistively heated evaporator. The 1ML thick samples were fabricated by sublimation of PTCDA molecules for 20 min at 400° C. The multilayer samples required a sublimation temperature of 420° C and an exposure time of 2 h, followed by a gentle thermal annealing at 140° C to flatten the molecular surface.

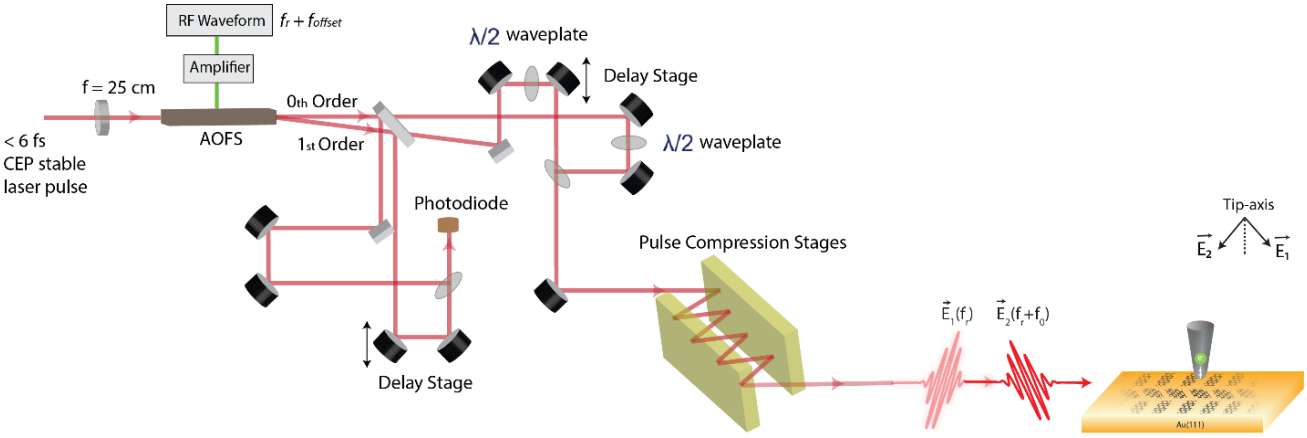

Extended data Fig. S1 | Experimental set-up. A p-polarized laser pulse is focused on an AOFS at Bragg angle, and the 0^{th} and 1^{st} order pulses are separated into two different arms of the Michelson-interferometer. Delay controlled pulses from the two arms of the interferometer are combined by a pellicle beam splitter. The pulses after the interferometer are compensated for their positive chirp by two sets of chirped dielectric mirrors before being directed to the STM junction.

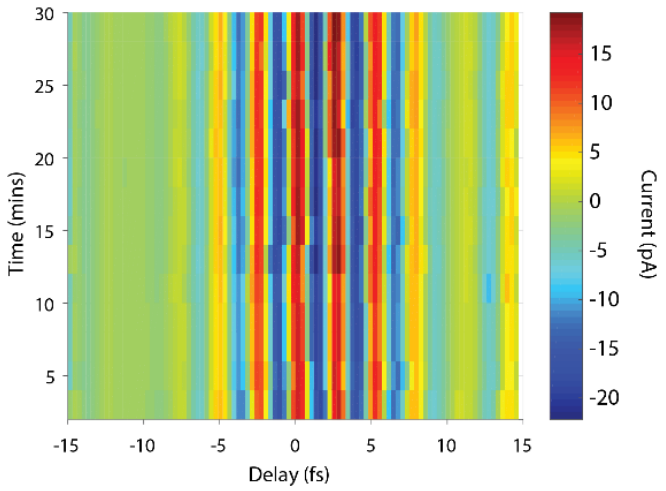

Extended data Fig. S2 | Long-term stability of the Michelson interferometer. A series of nonlinear cross-correlation traces of the laser-induced tunneling current at the STM junction acquired continuously over 30 mins.

II. Homodyne beating detection of the laser-induced tunneling current

The bandwidth of the STM used in the present work is limited to 1 kHz. The repetition rate of the laser (~ 80 MHz) is too high compared to the bandwidth of the STM. In order to lock-in detect the laser-induced tunneling current we have performed a homodyne beating of the tunneling current induced by the two laser pulses from the Michelson interferometer which come at slightly different carrier frequencies. The 0^{th} order beam after the AOFS (one arm of the interferometer) comes at the carrier frequency of the laser (f_r), and the 1^{st} order beam (other arm of the interferometer) comes at slightly higher carrier frequency ($f_r + f_0$). The two laser pulses are orthogonally polarized and both have an angle of ~ 45º with respect to the axis of the nanotip of the STM. Due to their orthogonal polarization, the two pulses only interfere along the direction of the nanotip. In the weak-field regime of interaction of the laser pulses at the STM junction, where the Keldysh parameter is > 1, two and three order photon processes, i.e. the 2^{nd} and 3^{rd} order nonlinear polarization, dominate the interaction of laser pulses. The net electric field of two pulses (E_1 and E_2) at a delay of τ between them at the STM junction can be written as;

$$E(t) = E_1(t)\exp(-if_r t) + E_2(t-\tau)\exp(-i(f_r + f_0)(t-\tau)).$$

Considering a 2nd order nonlinear polarization at the STM junction, the total polarization induced by the two pulses at the STM junction can be expressed as;

$$P_{NL}(t) \propto E(t)^2$$

$$P_{NL}(t) \propto E_1^2 \exp(-2if_r t) + E_2^2 \exp(-2i(f_r + f_0)(t-\tau)) + E_1(t) \times E_2(t-\tau) \exp(i(f_r + f_0)\tau + if_0 t) + \text{c.c.}$$

Here, the first two components of the non-linear polarization come at very high frequencies ($2f_r$ and $2(f_r + f_0)$) which cannot be measured by lock-in detection owing to the limited bandwidth of the STM. The current at such high frequencies is mixed with the tunneling current signal at 0 Hz in the STM. The cross-terms in the above equation come at the small offset frequency of f_0, the laser-induced tunneling current at this frequency can be lock-in detected.

$$P_{NL}(t)|_{f_0} = |E_1 E_2| \cos(f_0 t + (f_r + f_0)\tau)$$

The amplitude of the two pulses in the experiment were equal, simplifying the above equation as;

$$P_{NL}(t)|_{f_0} = |E^2| \cos(f_0 t + (f_r + f_0)\tau) .$$

At τ = 0 fs delay between the two pulses, the above equation imitates the polarization response induced by a single pulse coming at the repetition rate of the small offset frequency of f_0 at the STM junction.

The offset frequency f_0 is detected by homodyne beating of the 0th and 1st order diffracted beams in a photodiode (see Fig. S1) for reference frequency in the lock-in detection.

III. Ultrashort-laser driven orbital imaging

The spatially resolved laser-induced tunneling current was acquired simultaneously with the z-topography in the constant current operation mode of the STM. The offset frequency f_0, where we lock-in detect the laser-induced tunnel current is much higher than the feedback bandwidth (0-300 Hz) of the STM, thus, not affecting the operation of the STM. Individual panels in Fig. S3 and S4 show the z-topography and the laser-induced tunneling current at various biases of the STM junction. The time-constant in the lock-in detection was 3 ms and the time per pixel (per spatial point) during STM imaging was 6 ms.

In order to ascertain that the laser pulses at the STM junction do not field-dress the electronic levels of the PTCDA molecules or the Au (111) surface, which is what one would expect for very low intensities of the laser pulse, we have measured the z-topography of the molecules in presence and in absence of the laser pulse. Fig. S4 compares the z-topography in presence and in absence of the laser pulse as well as the spatial distribution of the laser-induced tunneling current for the HOMO and LUMO of the monolayer PTCDA molecules. Fig. S5 shows a comparison of simulated STM images (see section VI below for details) with the experimentally measured spatial variation of the laser-induced tunneling current for a monolayer of PTCDA molecules.

A large area z-topography scan of multilayer of PTCDA molecules is shown in Fig. S6. Monolayers of different thickness of PTCDA molecules can be seen. The experiments presented in Fig. 3 and 4 (main text) were performed on top of a four-monolayer thick multilayer area.

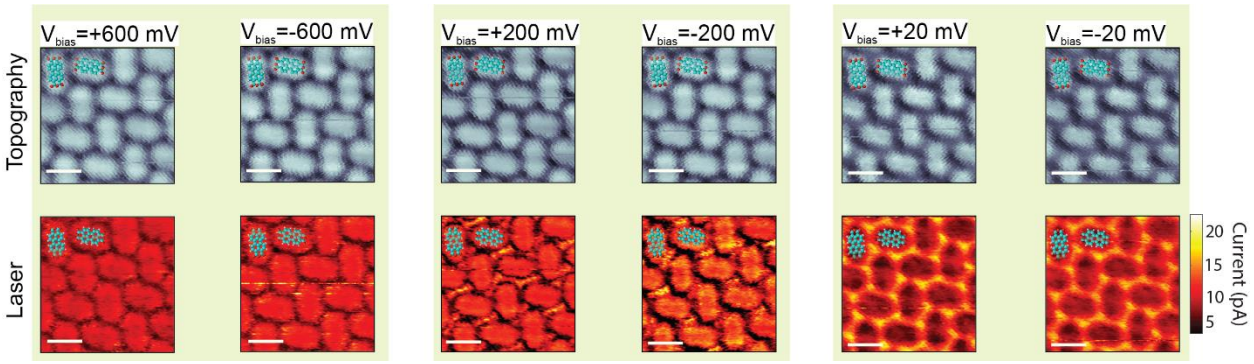

Extended data Fig. S3 | Ultrashort laser-driven orbital imaging. Comparison of z-topography and simultaneously acquired laser-induced tunneling current at various biases at the tunnel junction of the STM for a monolayer of PTCDA molecules on Au (111). Panels in the top row show the z-topography, whereas the panels in the bottom row show the spatial distribution of the laser-induced tunneling current. The bias at the tunnel junction is annotated on top of each panel. The scale bar in each panel denotes a spatial dimension of 1 nm.

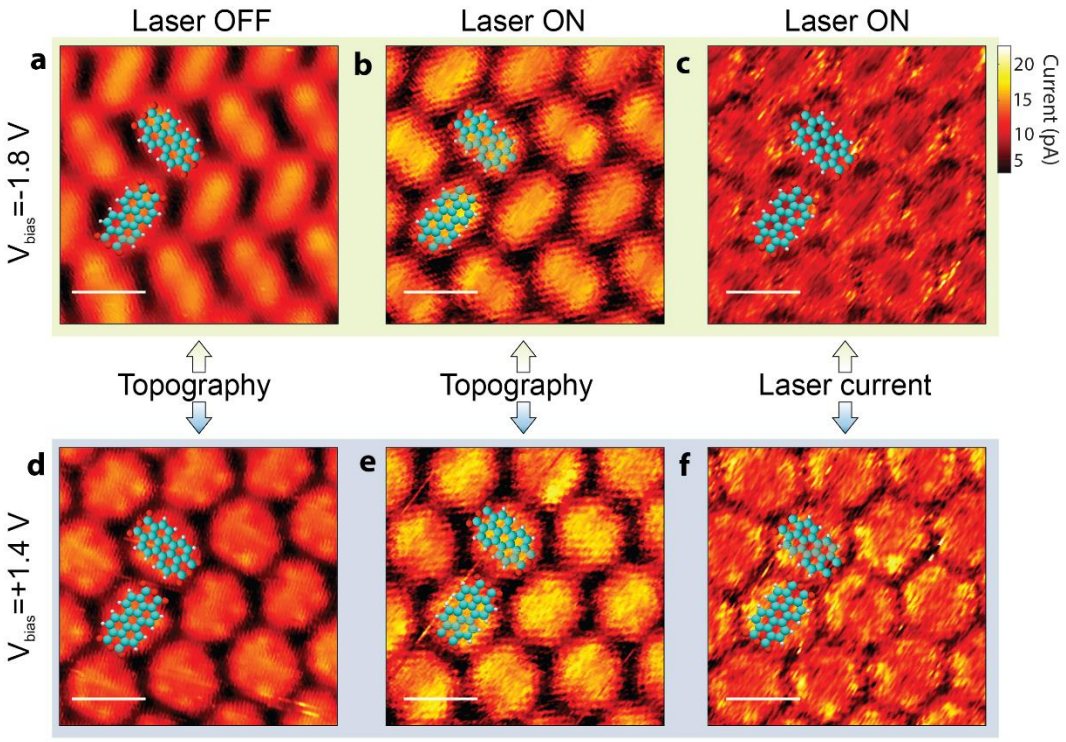

Extended data Fig. S4 | Ultrashort laser-driven orbital imaging. a, b, Comparison of the z-topography of the HOMO of a monolayer of PTCDA molecules on top of Au (111) in presence and in absence of the laser, respectively. **d, e,** Comparison of the z-topography of the LUMO of monolayer of PTCDA molecules on Au (111) surface in presence and in absence of the laser, respectively. **c, f,** Spatially resolved laser-induced tunneling current for the HOMO and LUMO, respectively. The scale bar in each panel denotes a spatial dimension of 1 nm.

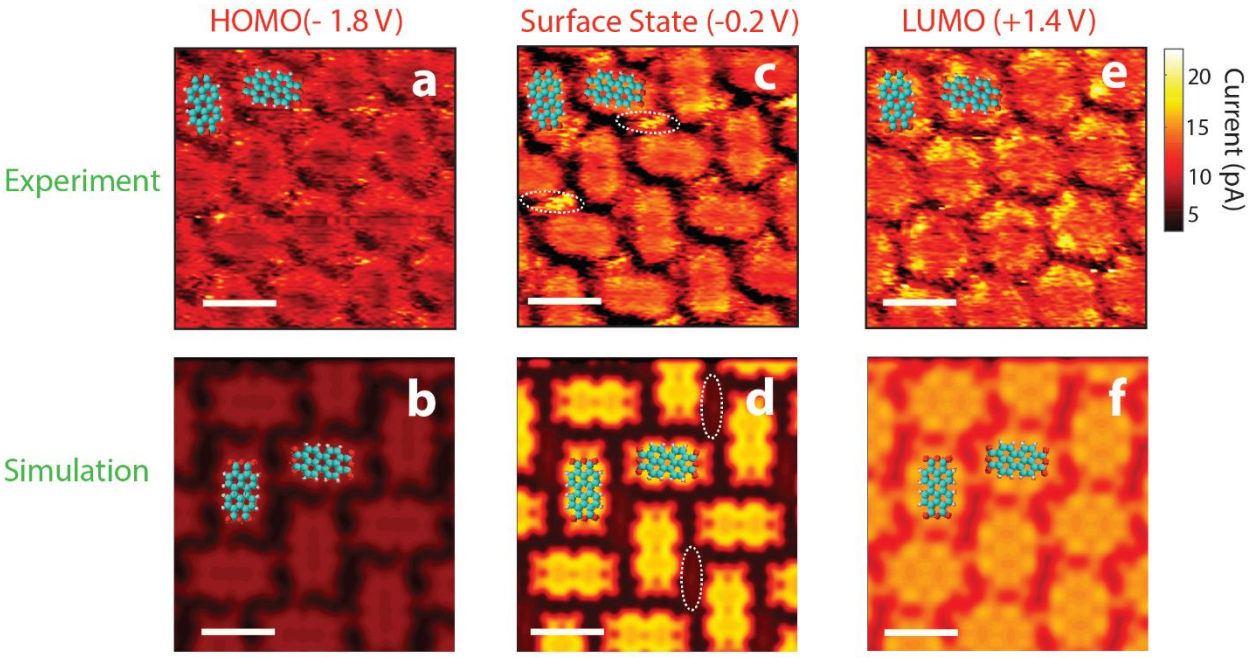

Extended data Fig. S5 | Comparison of simulated STM images with the experimentally measured spatial variation of the laser-induced tunneling current for a monolayer of PTCDA molecules. a, b, Comparison of the experimentally measured (**a**) spatial variation of the laser-induced tunneling current for the HOMO (-1.8 V) with the simulated STM image (**b**) (see section VI for details of the simulations). An oval shape distribution of the tunneling current intensity can be clearly seen in both cases. **c, d,** Comparison of the experimentally measured (**c**) spatial variation of the laser-induced tunneling current at a bias voltage of -200 mV with the simulated STM image (**d**). The intensity of the tunneling current between the molecules arising from the surface state is clearly visible. White dashed ellipses are to guide the eyes of the reader to the tunneling current intensity between the molecules in **c** and **d**. Please note that the signatures of the surface state in **c** and **d** are rotated by 90°. **e, f,** Comparison of the experimentally measured (**e**) spatial variation of the laser-induced tunneling current for the LUMO (1.4 V) with the simulated STM image (**f**). A hexagonal shape distribution of the tunneling current intensity can be clearly seen in both the cases, with some characteristic features on the edges. The scale bar in each panel denotes a spatial dimension of 1 nm. The color bar in the extreme right is only for the panels **a, c** and **e.**

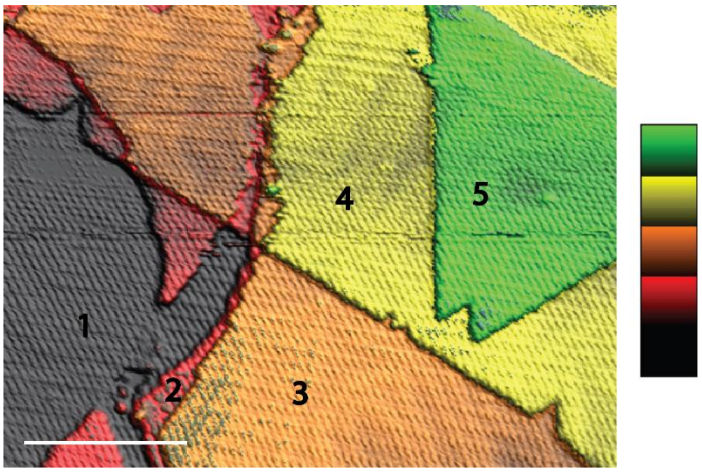

Extended data Fig. S6 | A large area z-topography scan of PTCDA multilayers grown on Au (111). The white scale bar at bottom of the figure denotes a spatial dimension of 20 nm. The numbers indicate layer thickness of monolayers.

IV. Space-time resolved quantum beating

The spatially resolved laser-induced tunneling current was recorded as a function of the delay between pump and probe pulses as shown in Fig. 2 and Fig. 4 in the main text. Here, we briefly explain the methodology used to measure such space-time scans. In the present experiment, the populations of the two dipole-coupled states oscillate π out of phase, implying that when the population in one state is higher, the population in the other state is correspondingly lower. To discard that these oscillations are due to the optical interference of the pulses when the delay is changed, we have recorded the laser-induced signal by lock-in detection in polar coordinates (R, θ) instead of in Cartesian coordinates (X, Y). All the results reported in this work have been obtained by measuring R, which only contains information about the phase associated with the beatings between the two electronic states. The phase associated with the optical interference appears in θ.

When the HOMO of the PTCDA molecules is lifted close to the Fermi level of the tip, a time-delayed pair of pump-probe pulses lead to a population exchange between the HOMO and the surface state according to Eq. 1 in the main-text. The different populations of the two states leave their signature in the spatial scan of the laser-induced tunneling current at every delay. These

spatial scans include, in addition, the static contribution from the current induced at the applied bias voltage in the presence of the two laser pulses. One can estimate this contribution from the spatial scans obtained in the single-pulse mode (zero delay), where there is barely any dynamic population exchange between the two levels (Fig. 1e, main text) and the measured laser-induced tunneling current mostly reflects the population of the lower electronic state. Therefore, this static contribution, which is present at all pump-probe delays, leads to a systematic static offset of the population dynamics in the HOMO, which must be removed. Nevertheless, this effect enables us to perform amplitude-selective filtering of the spatial distribution of the laser induced current in each space-time scan. Owing to the sharp contrast of the spatial distributions of the laser-induced tunneling current arising from the two states, we can transparently distinguish the electronic population in either of the states as a function of the delay. Here, the laser-induced tunneling current above the defined threshold in the amplitude-selective filtering will correspond to population of the HOMO, and below the threshold, to populations of the surface state. The topographic scans resulting from this amplitude-selective filtering procedure showing the temporal evolution of the HOMO and surface-state populations as a function of pump-probe delay are given in Fig. S7a and S7b, respectively. We note that the threshold for the amplitude-selective filtering is the same for all individual topographic scans in the space-time map. Integrating the individual spatial maps in Fig. S7a and S7b, we obtain the temporal evolution of the electronic population between the two states as shown in Fig. S8a. The offset-free temporal evolution of the population dynamics in the two states is shown in Fig. S8b, which is identical to Fig. 2f in the main text. This population dynamics can be conveniently translated into the occupation dynamics between the HOMO and the surface state as shown in Fig. S8c. Finally, the space-time scans shown in Fig. 2e (main text) are obtained by combining the spatial scan of the laser-induced tunneling current measured at zero delay with the information of the occupation and population dynamics displayed in Fig. S8b and c.

An analogous analysis was performed for the HOMO to LUMO electron dynamics in the 4-monolayer system. The spatio-temporal evolution of the laser-induced tunneling current for the LUMO and HOMO states during the electronic oscillation dynamics is shown in Fig. S9a and S9b, respectively. Here, the laser-induced tunneling current above the threshold in the amplitude-selective filtering for all the spatial maps will correspond to population of the HOMO, and below the threshold, to population of the LUMO. The amplitude-selective filtering is the same for all the

topographic scans. Integration of the spatio-temporal maps in Fig. S9 reveals the oscillation of the population between the HOMO (Fig. S9b) and LUMO (Fig. S9a) states as a function of the delay between pump and probe pulses, as displayed in Fig. S10a. The space-time scans shown in Fig. 4d (main text) were obtained by combining the spatial scan of the laser-induced tunneling current measured at zero delay with the information of the occupation and population dynamics displayed in Figs. S10a, S10b and S10c.

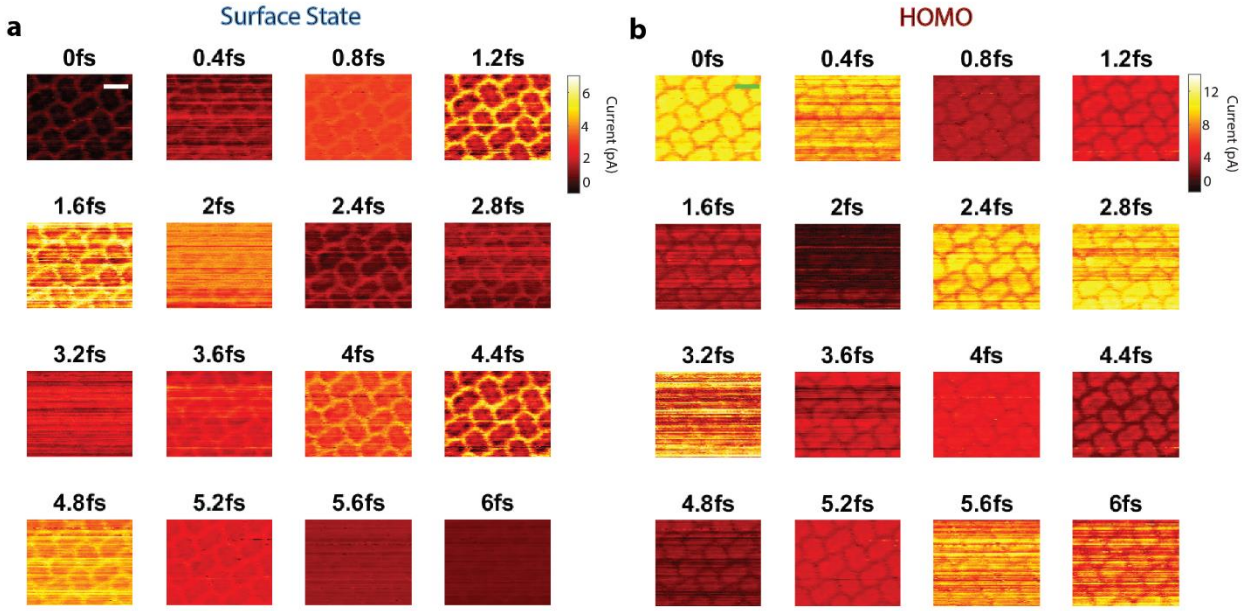

Extended data Fig. S7 | Space-time resolved quantum beating. a, b, Spatially resolved maps of the temporal evolution of the laser-induced tunneling current as a function of the delay between the pump and probe pulses for the surface state threshold (**a**) and the HOMO threshold (**b**) in the HOMO to surface state dynamics. The color axis is the same in all panels in **a** and **b** as shown in the top right corner for both of them. The delay between pump and probe pulses is annotated on top of each panel. The scale bar shown in the 1st panel of **a** and **b** is the same for all the plots and represents here a spatial dimension of 1 nm.

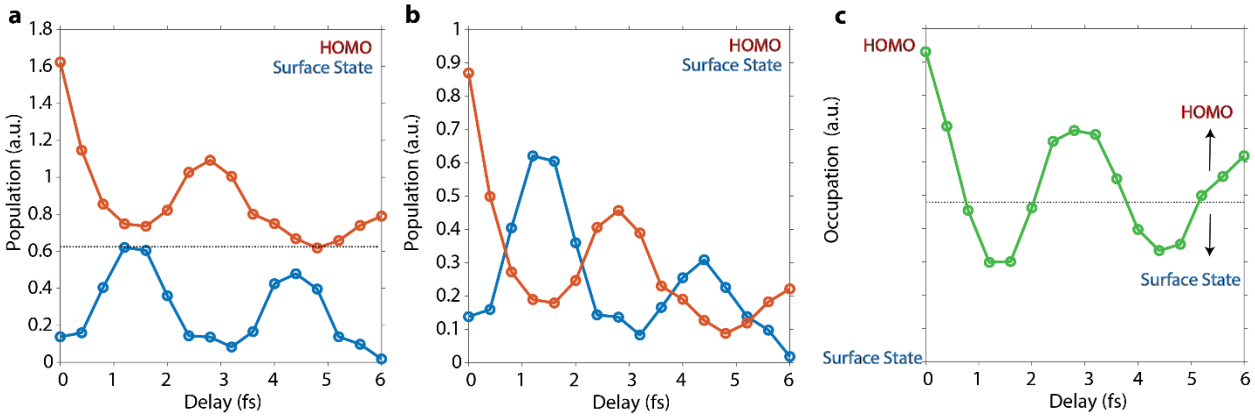

Extended data Fig. S8 | a, Temporal evolution of the population in the surface state and the HOMO for the HOMO-Surface state quantum beating, as obtained by integration of the laser-induced signal in the individual maps in Fig. S7a and S7b respectively. **b,** Population dynamics of the HOMO and surface-state after the offset correction. **c,** Occupation dynamics of the population in the HOMO and the surface-state as obtained by subtracting the curves shown in **b**.

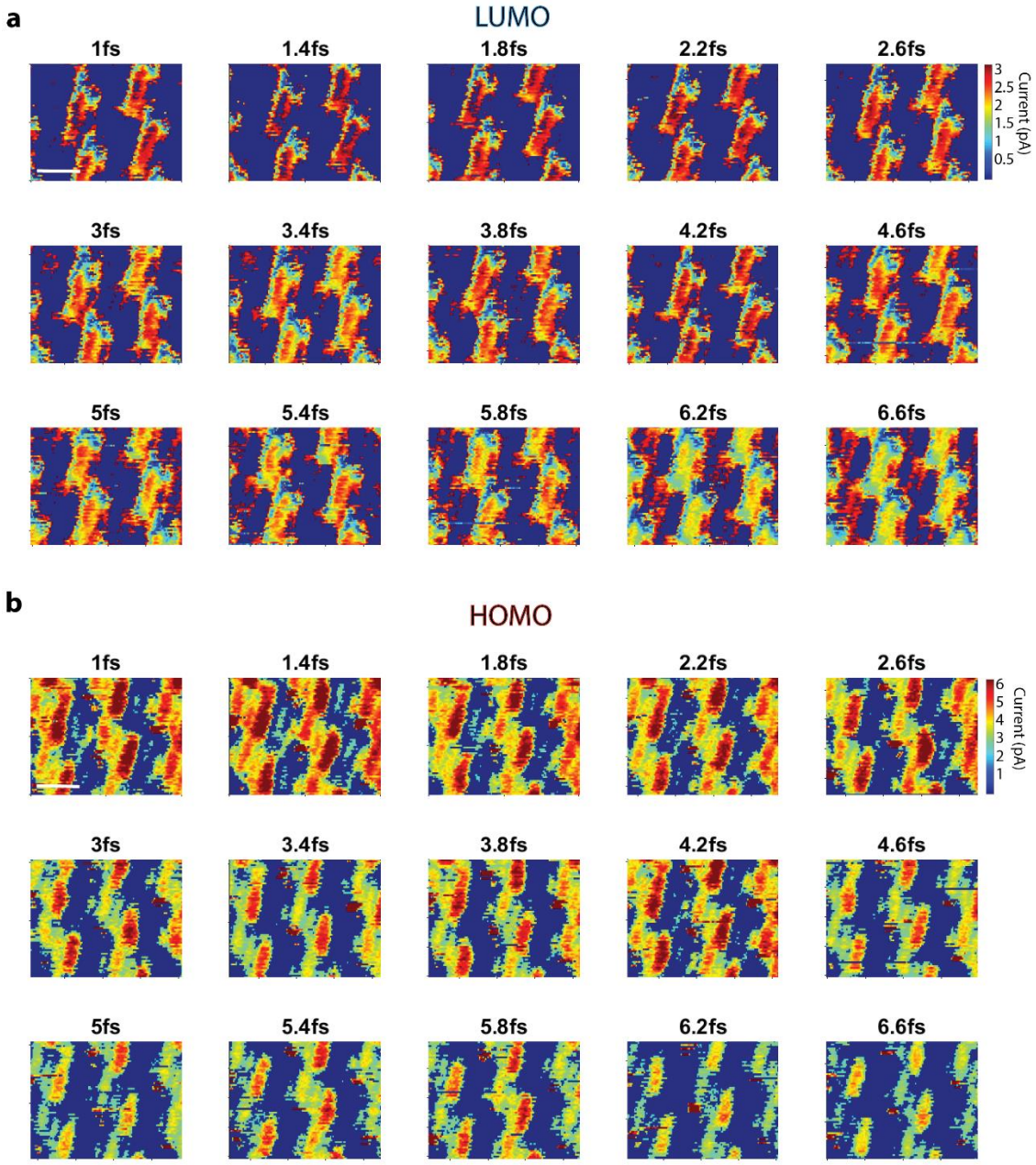

Extended data Fig. S9 | Space-time resolved oscillation between HOMO and LUMO. a, b, Spatially resolved maps of the temporal evolution of the laser-induced current as a function of the delay between pump and probe pulses for the LUMO (**a**) and the HOMO (**b**) states in the HOMO to LUMO dynamics of the 4-monolayer system. The color axis is the same in all panels in **a** and **b** as shown in the top right corner for both of them. The delay between the pump and probe pulses is annotated on top of each panel. The scale bar shown in the 1st panel of **a** and **b** is the same for all the plots and represents here a spatial dimension of 1 nm.

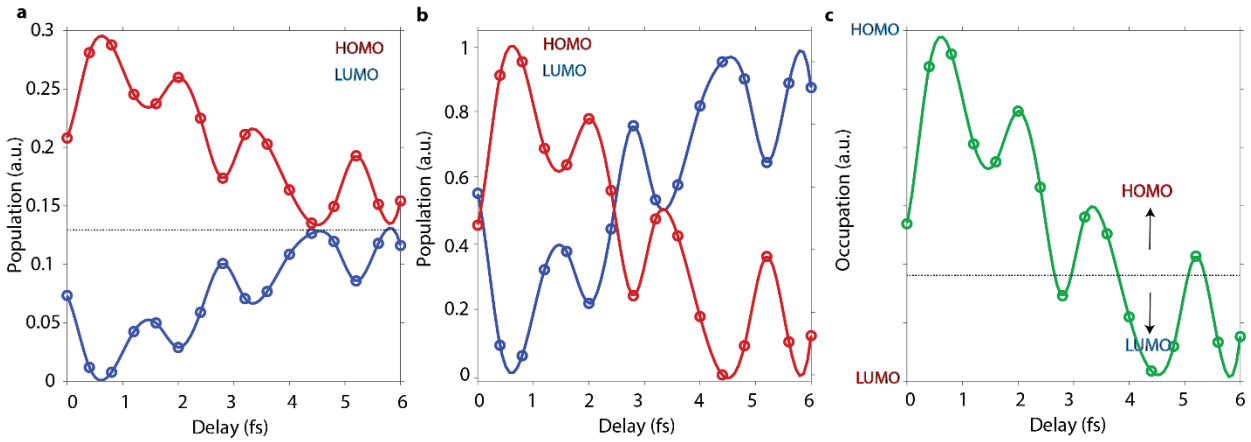

Extended data Fig. S10 | a, Temporal evolution of the population in the LUMO and the HOMO for the HOMO-LUMO dynamics in the 4-monolayer system, as obtained by integration of the laser-induced signal in the individual maps in Figure S9a and S9b respectively. **b,** Population dynamics of the HOMO and LUMO after the offset correction. **c,** Occupation dynamics of the population in the HOMO and the LUMO as obtained by subtracting the population dynamics curves in **b**.

V. Two-state model

We present here the derivation of a simple wave-function model to describe the dynamics generated by the combination of two identical time-delayed pulses in a resonantly-coupled two-level system. We will use atomic units throughout unless otherwise stated. For a two-level system subject to a time dependent external potential, the time-dependent Schrödinger equation

$$[\mathcal{H} + W(t)]\Psi(t) = i\frac{d}{dt}\Psi(t) \tag{1}$$

can be solved by expanding $\Psi(t)$ in the basis of the two eigenstates of $\mathcal{H}$, ψ_i and ψ_f, with associated eigenvalues ω_i and ω_f,

$$\Psi(t) = b_i(t)\psi_i e^{-i\omega_i t} + b_f(t)\psi_f e^{-i\omega_f t}. \tag{2}$$

Inserting Eq. (2) in Eq. (1) and projecting onto ψ_i and ψ_f leads to the system of coupled differential equations:

$$i\frac{d}{dt}b_i(t) = \mathcal{W}_{if}\, b_f(t) \tag{3}$$

$$i\frac{d}{dt}b_f(t) = \mathcal{W}_{fi}\, b_i(t), \tag{4}$$

where $\mathcal{W}_{if} = <\psi_i|W(t)|\psi_f>$ and, for simplicity, we have assumed that the potential $W(t)$ cannot couple a state with itself, i.e., $\mathcal{W}_{ii} = \mathcal{W}_{ff} = 0$ (this is the case for systems with no permanent dipole).

In the experiment, two identical pulses of duration T with orthogonal linear polarizations, each one forming an angle of 45° with the tip axis, impinge almost parallel to the surface (see Fig. S1). For convenience, we will decompose the electric field amplitudes of the pulses, $\boldsymbol{E}_1$ and $\boldsymbol{E}_2$, with $|\boldsymbol{E}_1|=|\boldsymbol{E}_2|=E$, in a parallel component to the surface plane (i.e., perpendicular to the plane formed by the incidence direction and the tip axis), $\boldsymbol{E}_1^{\parallel} = \left(E/\sqrt{2}\right)\boldsymbol{u}^{\parallel} \equiv \mathcal{E}\boldsymbol{u}^{\parallel}$ and $\boldsymbol{E}_2^{\parallel} = -\left(E/\sqrt{2}\right)\boldsymbol{u}^{\parallel} \equiv -\mathcal{E}\boldsymbol{u}^{\parallel}$, and a perpendicular component to the surface (i.e., parallel to the tip axis), $\boldsymbol{E}_1^{\perp} = \boldsymbol{E}_2^{\perp} = \left(E/\sqrt{2}\right)\boldsymbol{u}^{\perp} \equiv \mathcal{E}\boldsymbol{u}^{\perp}$. Hence, for the geometry of the experiment, the interaction potential can be written as,

$$W(t) = \mu^{\parallel}\mathcal{E}\left[\sin(\omega t) - \sin\left(\omega(t+\tau)\right)\right] + \mu^{\perp}\mathcal{E}\left[\sin(\omega t) + \sin\left(\omega(t+\tau)\right)\right] \quad \text{for } t \le \tau \le T \tag{5}$$

$$W(t) = 0 \quad \text{elsewhere}, \tag{6}$$

where ω is the laser frequency, τ is the pump-probe delay (or, equivalently, $\omega\tau$ is the phase difference between the two pulses in the overlapping region) and $\mu^{\parallel}$ and $\mu^{\perp}$ are, respectively, the parallel and perpendicular components of the transition dipole-moment matrix element.

For simplicity, we have assumed that the pulses overlap all the time between 0 and T, and have a perfectly rectangular envelope. Introducing a more sophisticated envelop is straightforward. Note that, for $\tau = 0$, the $\mu^{\parallel}$ contribution to $W(t)$ vanishes, while the $\mu^{\perp}$ contribution is identical to that obtained for a single pulse with a field amplitude $2\mathcal{E} = \sqrt{2}E$, i.e., $W(t) = \mu^{\perp}2\mathcal{E}\sin(\omega t)$. For a delay τ equal to half the period of the laser pulses, $\tau = \pi/\omega$, the situation is the opposite: the $\mu^{\perp}$ contribution vanishes, and the $\mu^{\parallel}$ one becomes $W(t) = \mu^{\parallel}2\mathcal{E}\sin(\omega t)$.

By substituting Eq. (5) in Eqs. (3) and (4), and applying the usual rotating wave approximation (which neglects the rapidly oscillating terms $\exp[i(\omega_{fi}+\omega)t]$), we obtain

$$\frac{d}{dt}b_i(t) = -\frac{1}{2}\left\{\left[e^{i(\omega-\omega_{fi})t} - e^{i(\omega-\omega_{fi})t}e^{i\omega\tau}\right]W_{if}^{\parallel} + \left[e^{i(\omega-\omega_{fi})t} + e^{i(\omega-\omega_{fi})t}e^{i\omega\tau}\right]W_{if}^{\perp}\right\}b_f(t) \quad (7)$$

$$\frac{d}{dt}b_f(t) = \frac{1}{2}\left\{\left[e^{-i(\omega-\omega_{fi})t} - e^{-i(\omega-\omega_{fi})t}e^{-i\omega\tau}\right]W_{if}^{\parallel} + \left[e^{-i(\omega-\omega_{fi})t} + e^{-i(\omega-\omega_{fi})t}e^{-i\omega\tau}\right]W_{if}^{\perp}\right\}b_i(t) \quad (8)$$

where $\omega_{fi} = \omega_f - \omega_i$ is the energy difference between the states *f* and *i*, $W_{if}^{\parallel} = \mu_{if}^{\parallel}\mathcal{E}$ and $W_{if}^{\perp} = \mu_{if}^{\perp}\mathcal{E}$, being $\mu_{if}^{\parallel}$ and $\mu_{if}^{\perp}$ the transition dipole matrix elements connecting the states ψ_i and ψ_f through $\mu^{\parallel}$ and $\mu^{\perp}$, respectively.

Under the present experimental conditions, we have $|W_{if}| \ll \omega_{fi}$. Therefore, we can assume that most of the laser induced dynamics is due to resonant transitions, i.e., only the frequency $\omega = \omega_{fi}$ contributes significantly (secular approximation). By applying this approximation, the above system of equations reduces to

$$\frac{d}{dt}b_i(t) = \left\{-\frac{1}{2}[1 - e^{i\omega_{fi}\tau}]W_{if}^{\parallel} - \frac{1}{2}[1 + e^{i\omega_{fi}\tau}]W_{if}^{\perp}\right\}b_f(t) \quad (9)$$

$$\frac{d}{dt}b_f(t) = \left\{\frac{1}{2}[1 - e^{-i\omega_{fi}\tau}]W_{if}^{\parallel} + \frac{1}{2}[1 + e^{-i\omega_{fi}\tau}]W_{if}^{\perp}\right\}b_i(t). \quad (10)$$

Inserting the derivative of Eq. (9) in Eq. (10), integrating from $t = 0$ to $t = T$ the resulting second order differential equation with the boundary conditions $b_i(0) = 1$ and $b_f(0) = 0$, and assuming that $\mu_{if}^{\parallel}$ and $\mu_{if}^{\perp}$ are real quantities, we obtain

$$b_i(T) = \cos\left[\mathcal{E}T\left\{\left|\mu_{if}^{\parallel}\right|^2\sin^2\left(\frac{\omega_{fi}\tau}{2}\right) + \left|\mu_{if}^{\perp}\right|^2\cos^2\left(\frac{\omega_{fi}\tau}{2}\right)\right\}^{1/2}\right] \quad (11)$$

and the corresponding probability

$$\wp_i(T) = \cos^2\left[\mathcal{E}T\left\{\left|\mu_{if}^{\parallel}\right|^2\sin^2\left(\frac{\omega_{fi}\tau}{2}\right) + \left|\mu_{if}^{\perp}\right|^2\cos^2\left(\frac{\omega_{fi}\tau}{2}\right)\right\}^{1/2}\right] \quad (12)$$

For state *f*, the probability is given by

$$\wp_f(T) = 1 - \wp_i(T) = \sin^2\left[\mathcal{E}T\left\{\left|\mu_{if}^{\parallel}\right|^2\sin^2\left(\frac{\omega_{fi}\tau}{2}\right) + \left|\mu_{if}^{\perp}\right|^2\cos^2\left(\frac{\omega_{fi}\tau}{2}\right)\right\}^{1/2}\right] \quad (13)$$

Eqs. (12) and (13) have been derived by assuming that the states *i* and *f* have an infinite lifetime. Assuming that the *i* and *f* states have an identical finite lifetime $1/\Gamma$ (which is supported by the scanning tunneling spectra given in the main text and methods), a similar derivation by using the non-Hermitian Hamiltonian $\mathcal{H}' = \mathcal{H} - i\Gamma/2$ with eigenvalues $\omega_{i,f} = \omega_{i,f} - i\Gamma/2$ leads to

$$\wp_i(T) = \cos^2\left[\mathcal{E}T\left\{\left|\mu_{if}^{\parallel}\right|^2 \sin^2\left(\frac{\omega_{fi}\tau}{2}\right) + \left|\mu_{if}^{\perp}\right|^2 \cos^2\left(\frac{\omega_{fi}\tau}{2}\right)\right\}^{1/2}\right] e^{-\Gamma\tau} \tag{14}$$

$$\wp_f(T) = \sin^2\left[\mathcal{E}T\left\{\left|\mu_{if}^{\parallel}\right|^2 \sin^2\left(\frac{\omega_{fi}\tau}{2}\right) + \left|\mu_{if}^{\perp}\right|^2 \cos^2\left(\frac{\omega_{fi}\tau}{2}\right)\right\}^{1/2}\right] e^{-\Gamma\tau} \tag{15}$$

We note that for $\tau = 0$ (the single pulse case discussed in the main text) and $\Gamma = 0$, we obtain the Rabi-like formulas

$$\wp_i(T) = \cos^2\left[\left|\mu_{if}^{\perp}\right|\mathcal{E}T\right] \tag{16}$$

$$\wp_f(T) = \sin^2\left[\left|\mu_{if}^{\perp}\right|\mathcal{E}T\right] \tag{17}$$

In the systems considered in this work, the perpendicular component of the dipole transition matrix element $\mu_{if}^{\perp}$ is always much smaller than the parallel one $\mu_{if}^{\parallel}$. Therefore, one can reasonably assume that $\mu_{if}^{\perp} = 0$ and Eqs. (14) and (15) reduce to

$$\wp_i(T) = \cos^2\left[\mathcal{E}T\left|\mu_{if}^{\parallel}\right|\sin\left(\frac{\omega_{fi}\tau}{2}\right)\right] e^{-\Gamma\tau} \tag{18}$$

$$\wp_f(T) = \sin^2\left[\mathcal{E}T\left|\mu_{if}^{\parallel}\right|\sin\left(\frac{\omega_{fi}\tau}{2}\right)\right] e^{-\Gamma\tau} \tag{19}$$

VI. Density functional theory calculations

VI.1 Technical details

Density Functional Theory (DFT) calculations were carried out within the Projector Augmented Wave (PAW) method[1] as implemented in the VASP code[2-4]. In all calculations we employed the PBE exchange-correlation functional[5] and included the Tkatchenko-Sheffler correction[6] to account for weak dispersion forces. The plane waves cut off energy was set to 400 eV, the self consistent cycle tolerance to 10^{-5}eV, whereas the 1st Brillouin Zone integration was carried out adopting Γ centered Monkhorst-Pack grids[7] characterized by at least $\Delta k \sim 0.1 \text{Å}^{-1}$. We analyzed

monolayer and 4-Layer of PTCDA slabs, both in the freestanding form and adsorbed on Au (111). In the latter case, the Au surface was modelled by a pre-optimized 4-layer thick Au slab with the suitable molecular system adsorbed on one side. Whenever an accurate description of the gold surface state was necessary, we adopted 15-layer thick Au slabs. In all calculations, the out-of-plane lattice constant was set so that a vacuum region of, at least, 20 Å was present. The simulated STM images were calculated by using the Tersoff-Hamann method[8].

Following the existing literature[9,10] and guided by the experimental STM images, we limited our analysis to molecular arrangements with rectangular or almost rectangular unit cells. Each unit cell contains two molecules in an L-shaped arrangement (see Fig. S11a). It is worth mentioning that, for the freestanding molecular systems, several choices are possible for the in-plane unit cell vectors (orientation and length), however, we focused our investigation to choices that were commensurable with the Au (111) surface. Hence, in our study we employed the following three in-plane unit cells (all lengths in Å):

Cell-1: $\begin{matrix}\boldsymbol{a}_1=\{20.195,0\}\\ \boldsymbol{a}_2=\{0,14.991\}\end{matrix}$ in which the lattice vectors are perpendicular and have a ratio of 1.35; this cell corresponds to the $\begin{pmatrix}7 & 0\\ -3 & 6\end{pmatrix}$ reconstruction of the Au (111) surface.

Cell-2: $\begin{matrix}\boldsymbol{a}_1=\{14.425,0\}\\ \boldsymbol{a}_2=\{0,19.988\}\end{matrix}$ in which the lattice vectors are perpendicular and have a ratio of 1.39; this cell corresponds to the $\begin{pmatrix}5 & 0\\ -4 & 8\end{pmatrix}$ reconstruction of the Au (111) surface.

Cell-3: $\begin{matrix}\boldsymbol{a}_1=\{12.983,2.498\}\\ \boldsymbol{a}_2=\{-2.885,19.988\}\end{matrix}$ in which the lattice vectors form an 87° angle and their lengths have a ratio of 1.53; this cell corresponds to the $\begin{pmatrix}4 & 1\\ -5 & 8\end{pmatrix}$ reconstruction of the Au (111) surface.

For each choice, we took into account several different initial starting configurations for the molecules. In all cases, we optimized the geometry of the system relaxing the coordinates of all the atoms of the molecules and of the topmost Au layer (when present) until the maximum force on the active atoms was less than 0.01 eV/Å.

VI.2 Energetics

		Monolayer	4-Layer		
		Total Energy (eV)	Total Energy (eV)	E/L (eV)	InterL E (eV)
Cell-1	Geo-1	-576.624 (flat)	-2314.9785	-578.745	-8.48
	Geo-2	-576.607	-2315.1444	-578.786	-8.65
Cell-2	Geo-1	-576.738 (flat)	-2313.5229 (flat)	-578.381	-6.57
	Geo-2	-567.736	-2315.8483	-578.962	-8.90
Cell-3	Geo-1	-577.011 (flat)	-2313.8400 (flat)	-578.710	-6.80
	Geo-2	-577.015 (flat)	-2317.3901	-579.348	-9.35
	Geo-3	-577.071	-2317.4477	-579.362	-9.40

Table.1: Energy information for the freestanding Monolayer and 4-Layer systems. For the four layer, the Energy per Layer is defined as $\mathrm{E/L} = \frac{1}{4}\mathrm{Total\ Energy}$; the "Interlayer Energy" is defined as: $\mathrm{InterL\ E} = \mathrm{Tot.\,En.\,(4Layer)} - 4 \times \mathrm{Tot.\,En.\,(Monolayer)}$.

In Table 1 we collect the energy information on the freestanding monolayer and the four monolayers of PTCDA molecules for the different unit cells included in this analysis. The energies given in the table correspond to equilibrium configurations (i.e. local minima in the configuration space). In the monolayer case, the results labeled with "flat" correspond to a final geometry in which the monolayer showed no appreciable rumpling; in the other geometries a sizeable (> 0.1Å) rumpling was observed. Comparing the total energies for the monolayer case, we can conclude that flat and non-flat geometries are equally stable. In the 4-Layer systems, the "flat" geometries are also characterized by "perfect" vertical stacking of the molecular layers. In the non-flat geometries, on the other hand, lateral displacements of successive molecular layers as high as 1.5Å are observed; these geometries are also characterized by a higher interlayer energy and a smaller overall thickness of the slab. We notice that individual layers in the 4-Layer systems are significantly more stable than the monolayer ones, due to the additional stability provided by the intralayer interaction. A comparative look at Table1 shows that the unit cell "Cell-3" is the choice that leads to the most stable configurations.

	Monolayer		4-Layer	
	Total Energy(eV)	Binding En. (eV)	Total Energy (eV)	Binding En. (eV)
Cell-1	-1141.4968	-4.91	-2880.8191	-5.71
Cell-2	-1114.7431	-4.70	-2854.2962	-5.15
Cell-3	-1075.1857	-4.87	-2816.3929	-5.64

Table.2 Energy information for the Monolayer and 4-Layer systems adsorbed on a 4-Layer thick slab of Au(111). The binding energy is defined as follows; $\text{Binding En.} = \text{Total Energy} - (\text{E}_{\text{Au}} - \text{E}_{\text{Freestanding Mol.}})$; a negative value of the binding energy is found whenever the adsorption of the system on gold is energetically favorable.

In Table 2 we report the energy information for the monolayer and 4-Layer PTCDA molecules adsorbed on a 4-Layer thick slab of Au (111). Both in the monolayer and the 4-Layer cases the metal-molecule interaction is rather weak, with the molecules stabilized at ~3.3 Å from the gold surface; in all cases the adsorption is energetically favorable. Due to the different unit cells, the Au slabs used for each case have a different number of Au atoms. This fact makes it impossible to compare the total energies across different unit cells. Nevertheless, we observe that the binding energies in all the cases are comparable, which means that we can assume the same stability ranking as for the freestanding case, i.e., we can conveniently assume that Cell-3 is the most stable configuration by a significant amount of energy. In Fig. S11 we report additional geometry information for Cell-3. Similar information for the Cell-1 and Cell-2 cases is available upon request.

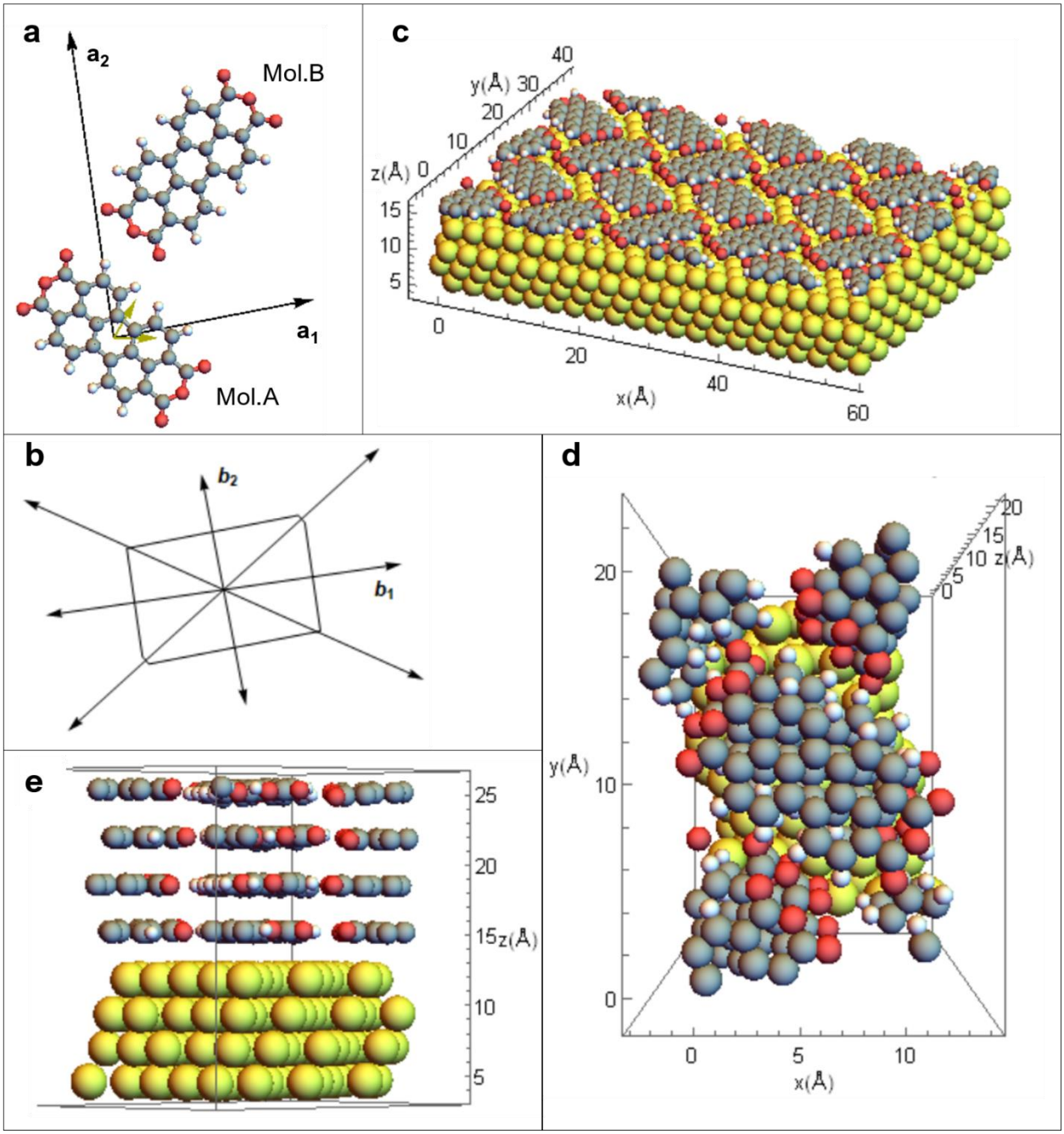

Fig. S11: Geometry information. a, PTCDA dimer made of two inequivalent molecules (Mol.A and Mol.B) which enter in the minimal unit cell of all the geometries analyzed in this work. We also show (to scale) the in-plane translation vectors of Cell-3 (long black arrows) and the in-plane lattice vectors of (1 × 1)Au(111) (short yellow arrows). **b**, In-plane reciprocal lattice vectors and first Brillouin Zone for the Cell-3 geometry. **c,** Equilibrium position of a Monolayer PTCDA adsorbed on Au(111) corresponding to the Cell-3 geometry; the x, y, and z axes are parallel to the [110], [100], and [111] crystallographic directions of gold, respectively. **d**, Top view of the equilibrium position of a 4-Layer PTCDA adsorbed on Au(111)

corresponding to the Cell-3 geometry; only the atoms of the minimal unit cell are shown for clarity. The fact that more than one molecular layer is visible from above is due to the non-perfect vertical stacking of the molecular layers (see also panel **e**). Lateral displacements as high as 1.5Å between the layers are observed. These displacements are compatible with the book-like stacking of the layers observed in the STM experiments. **e**, Side view of the equilibrium position of a 4-Layer PTCDA adsorbed on Au(111) corresponding to the Cell-3 geometry. The overall thickness of the 4-Layer molecular slab is ~ 10Å, whereas the average distance between the topmost Au layer and the bottommost PTCDA layer is ~ 3.4Å. Each molecular layer is not perfectly planar. The bottommost molecular layer exhibits the highest value of the rumpling $Max\{z\} - Min\{z\} = 0.6$Å; for the other molecular layers the rumpling is ~ 0.3Å.

VI.3 Simulated DOS and STM images

In Fig. S12a we show the total density of states (DOS) and the projected density of states (pDOS) as calculated by DFT for a PTCDA monolayer adsorbed on a 15-layer thick Au(111) slab; in the same panel we also show the total DOS of a freestanding PTCDA monolayer (dashed blue line). We start the analysis from the latter. The unit cell contains two inequivalent molecules. This fact is reflected in the DOS peaks corresponding to the HOMO and LUMO orbitals (a sketch of the HOMO and LUMO orbitals for the isolated PTCDA is given in Fig. S12b), which appear as double peaks. The energy separation between the HOMO and LUMO "groups" is of the order of 1.5 eV. We observe that this energy separation is comparable to the HOMO-LUMO gap in the isolated PTCDA molecule as calculated by DFT. It is important to mention that, for all the systems analyzed in this work, the DFT-predicted values of the HOMO-LUMO gap underestimate the experimental values. This is a well known shortcoming of DFT approaches, mainly due to the difficulty to describe the energy of the unoccupied states (see for instance J. Phys. Chem. A 2007, 111, 1554-1561). Usually, such problems are mitigated by employing post-DFT methods and other advanced theories. However, these methods are computationally much more expensive and are therefore out of reach for a systematic investigation of systems as big as those considered in the present work.

The pDOS shown in Fig. S12a show that the presence of the metal surface reduces the energy separation within the HOMO or LUMO groups, while leaving practically unchanged the HOMO-LUMO gap. We further observe that the peaks are slightly broadened, which is due to the "hybridization" of the molecular orbitals with the gold substrate. More insight into this effect is

gained by looking at Figs. S12c, d, in which we plot the probability density as a function of "z" for the one electron states having high HOMO or LUMO "character". As can be seen, due to the presence of the gold substrate, it is not possible to assign the HOMO or LUMO label to a single one-electron state. In fact, for the one-electron states belonging to the so-called HOMO and LUMO groups, a significant portion of the wavefunction leaks inside the gold slab. The tables shown in Figs. S12f, g, give the weights of the HOMO and LUMO components in the one-electron states contributing to the HOMO and LUMO groups shown in panels c and d, respectively.

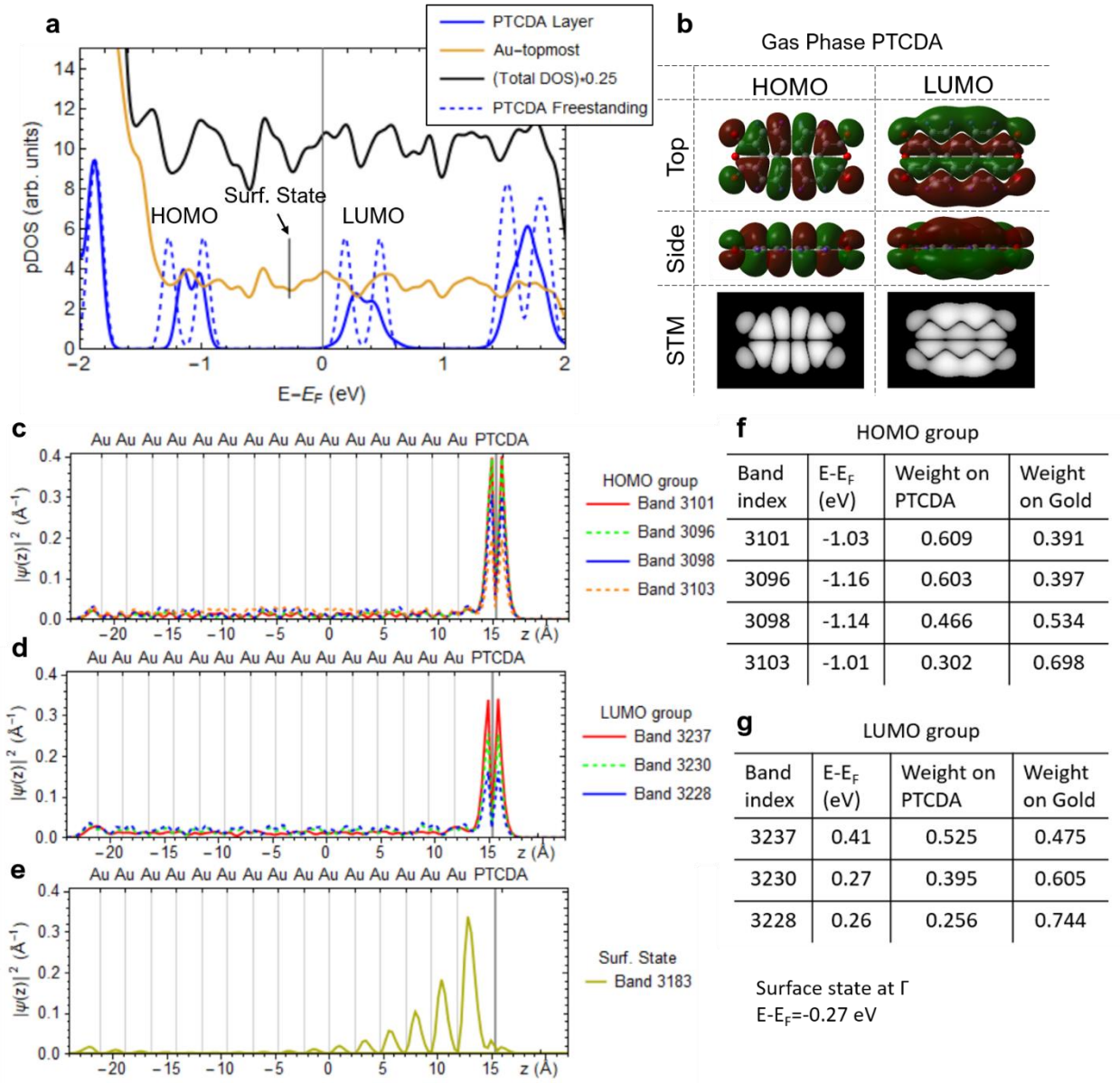

f HOMO group

Band index	E-E$_F$ (eV)	Weight on PTCDA	Weight on Gold
3101	-1.03	0.609	0.391
3096	-1.16	0.603	0.397
3098	-1.14	0.466	0.534
3103	-1.01	0.302	0.698

g LUMO group

Band index	E-E$_F$ (eV)	Weight on PTCDA	Weight on Gold
3237	0.41	0.525	0.475
3230	0.27	0.395	0.605
3228	0.26	0.256	0.744

Surface state at Γ
E-E$_F$=-0.27 eV

Fig. S12 | Monolayer PTCDA on Au(111). **a**, Calculated total DOS and projected DOS on different groups of atoms for a Monolayer PTCDA adsorbed on a 15-Layer thick Au(111) slab. In the same panel,

the total DOS of a freestanding Monolayer PTCDA is also included (blue dashed line); the same broadening in all the plots was used to ease comparison; the Fermi level of the freestanding case has been chosen so that the MOs in the two cases were aligned. **b**, HOMO and LUMO orbitals of an isolated PTCDA molecule (red 0.002 isosurface; green -0.002 isosurface); top views, a side views and the simulated STM images are given. **c-e**) Probability density along the out-of-plane direction, $|\psi(z)|^2$, corresponding to representative one-electron states, at the Γ point, for the Monolayer-PTCDA/15-Layer-Au(111) system; **c**: one-electron states with high "HOMO-character"; **d**: one-electron states with high "LUMO-character"; **e**: the gold surface state. **f**, Weights of the HOMO components in the one-electron states of the HOMO group given in panel c on two spatial regions comprising either the PTCDA monolayer or the gold slab. **g** Same as **f** for the LUMO group.

Turning our attention to gold, we observe that the gold surface state gives rise to a small peak in the DOS, which is barely detectable in the pDOS of the topmost gold layer (the onset of the surface state is marked by a vertical line in Fig.S12a). In Fig. S12e we plot the probability density as a function of "z" for the surface state at the Γ point. Interestingly, the plot in Fig.S12e shows that the presence of the molecular layer has an influence on the surface state, as its tail is slightly enhanced compared to that found in the pure Au (111) surface.

The assignment of the pDOS peaks to the HOMO or LUMO groups is corroborated by the simulated STM image of the Monolayer PTCDA adsorbed on gold shown in Fig. S13a, c. Indeed, setting the bias voltage to $V_B = -1.5V$, the entire so-called HOMO group is included in the integration of the electronic density. By direct comparison with Fig.S12b, we conclude that the resulting simulated STM images in Fig. S13a is made of "HOMO" orbitals localized on the two inequivalent molecules of the unit cell. A similar argument holds for $V_B = 0.6V$ and the LUMO orbitals. A very interesting image is obtained by setting $V_B = -0.5V$, in Fig. S13b. In this latter case, the $E_F - eV_B$ energy window does not incorporate any molecular state. On the other hand, it fully includes the energy dispersion of the filled part of the gold surface state. The resulting simulated STM image hence shows the surface state as a smooth structure between the molecules. Interestingly enough, for this bias voltage the molecules are still visible because their presence enhances the tail of the surface state (Fig. S12e), nevertheless their appearance does not resemble any molecular orbital.

To complete the study of the PTCDA monolayer, we report in Fig. S13d-f the simulated STM images for the freestanding monolayer. A direct (vertical) comparison between Fig. S13a, c and

Fig. S13d, f demonstrates that, indeed, the presence of the metal surface does not affect much the features of the PTCDA monolayer. As expected, for $V_B = -0.5V$, nothing is found in the simulated STM image of the freestanding PTCDA monolayer, because the integration window does not incorporate any electronic state.

We complete our study by analyzing the electronic properties of the 4-Layer system adsorbed on a 4-Layer Au (111) slab. In Fig. S14a we report the pDOS for such system: we projected the DOS on each molecular layer (the plots are vertically displaced for clarity) and on the topmost Au layer. Within each molecular layer, we further divided the contribution to the pDOS among the two inequivalent molecules of the layer. The 4-layer system has a total of 8 molecules, hence we expect 8 HOMO like orbitals and 8 LUMO like orbitals. Due to the broadening employed in the pDOS plot and, since some of these one-electron states are close in energy, it is not possible to fully resolve this fine structure into 8 pDOS peaks. However, within each molecular layer, the contribution to the pDOS coming from the inequivalent molecules is well resolved. An important consequence of this result is that an educated choice of the bias voltage, besides imaging the HOMO or the LUMO of the molecules of the topmost layer, can also be used to selectively image a selected group of molecules. This fact is corroborated by the simulated STM images for positive and negative biases given in Fig. S14b, e. If the bias voltage is set to $V_B = -1.0V$, the HOMO of only one of the two inequivalent molecules (Mol.B) is imaged, whereas the other molecule remains dark. On the other hand, for $V_B = 0.4V$, the opposite is found: the LUMO orbital of Mol.A is imaged whereas Mol.B is dark. We further notice that Mol.A and Mol.B are organized in molecule "strips" that, setting the appropriate bias voltage, can appear as bright or dark. Such a feature is reminiscent of what is found in the experimental images (see Fig. 3, main text). We further observe that, if the bias voltage is high enough (in absolute value) so that all the molecular states are included in the integration window (Fig. S15c, e), all molecules present the same brightness and all the LUMO (or HOMO for negative biases) of all the topmost molecules are imaged. We conclude by noticing that the molecules' rumpling also leaves its signature in the simulated STM images: one side of each molecule presents a higher apparent height than the other side.

In Fig.S16 we report the pDOS and the simulated STM images for a self standing 4-Layer PTCDA system. A direct comparison between Fig. S15 and Fig. S16 shows that the presence of the gold substrate induces only minor differences in the pDOS plot, with the strongest effect on the

bottommost layer of molecules, which is in direct contact with the Au surface. Interestingly, the simulated STM images present identical features.

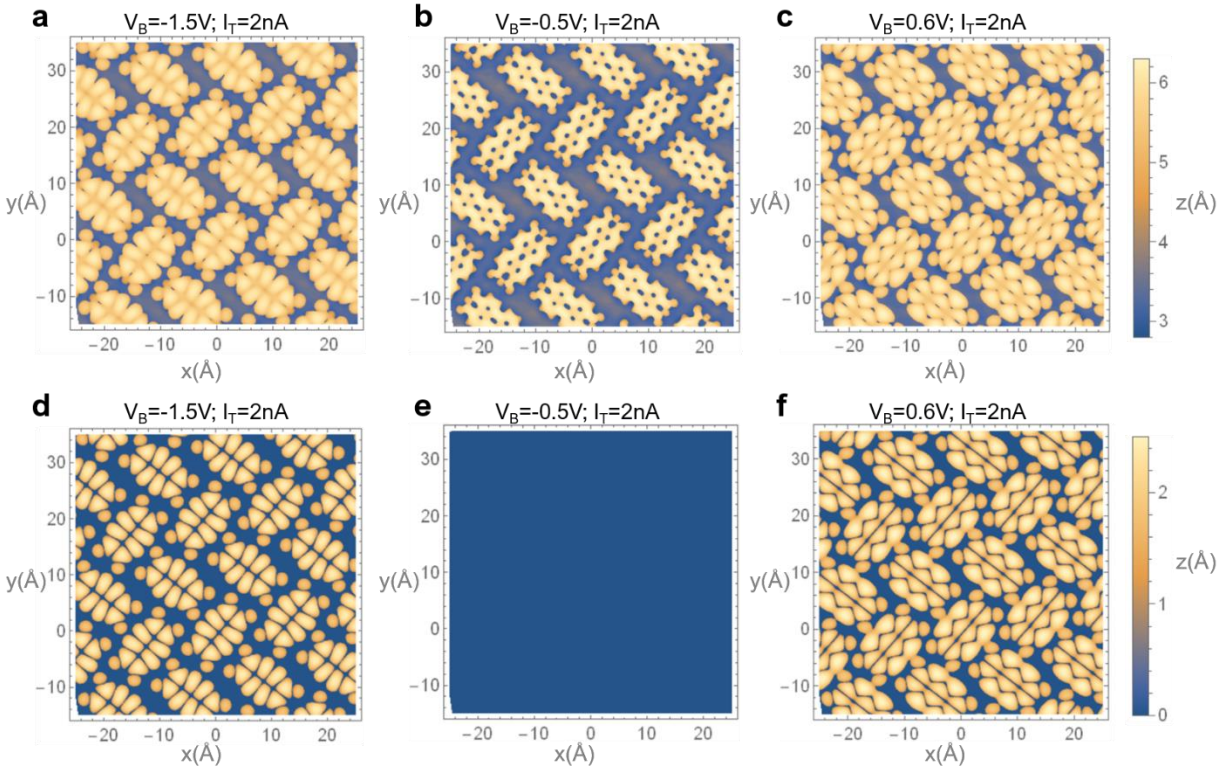

Fig. S13 | Monolayer PTCDA: Simulated STM images. **a, b, c,** Simulated STM images for a Monolayer PTCDA adsorbed on a 15 Layer thick Au (111) slab for three different values of the bias voltage. **d, e, f**, Simulated STM images for a freestanding Monolayer PTCDA; the same tunneling parameters as in panels **a-c** are used to ease comparison.

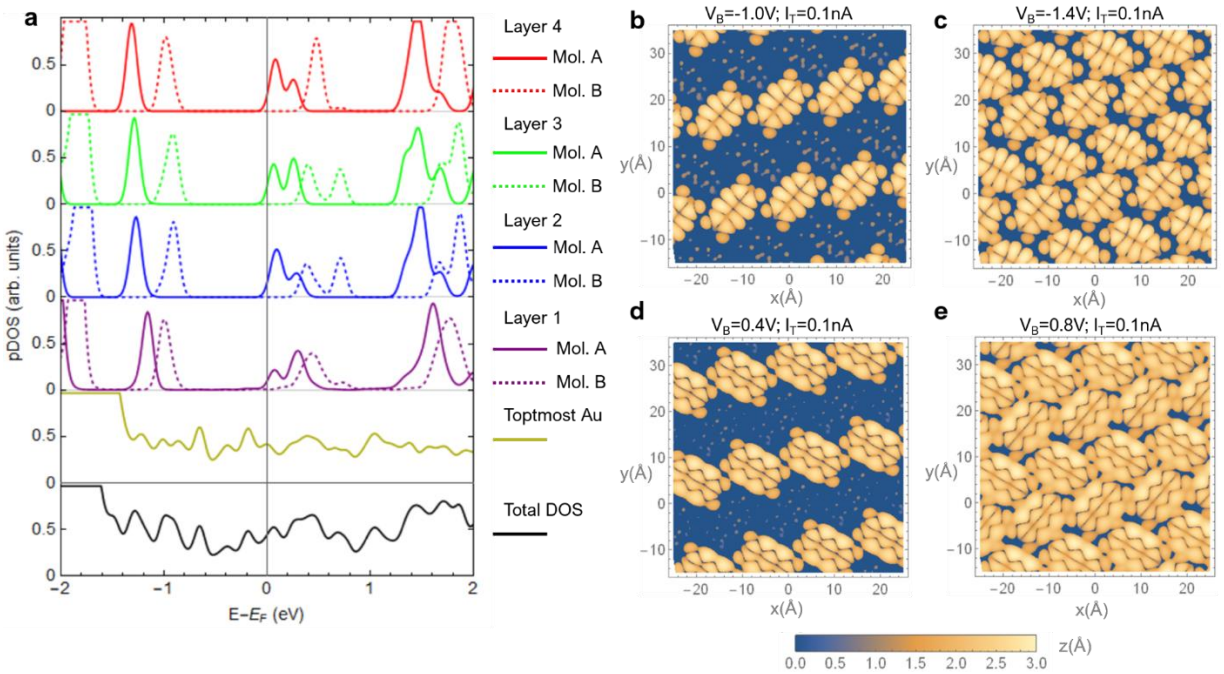

Fig. S14 | 4-Layer PTCDA on Au (111). a, Calculated total DOS and projected DOS on different groups of atoms for a 4-Layer PTCDA system adsorbed on a 4-Layer thick Au (111) slab. The pDOS of different molecular layers and the topmost Au layer are shown; within each molecular layer, the pDOS is further projected onto the two inequivalent molecules. **b-e**, Simulated STM images at different biases.

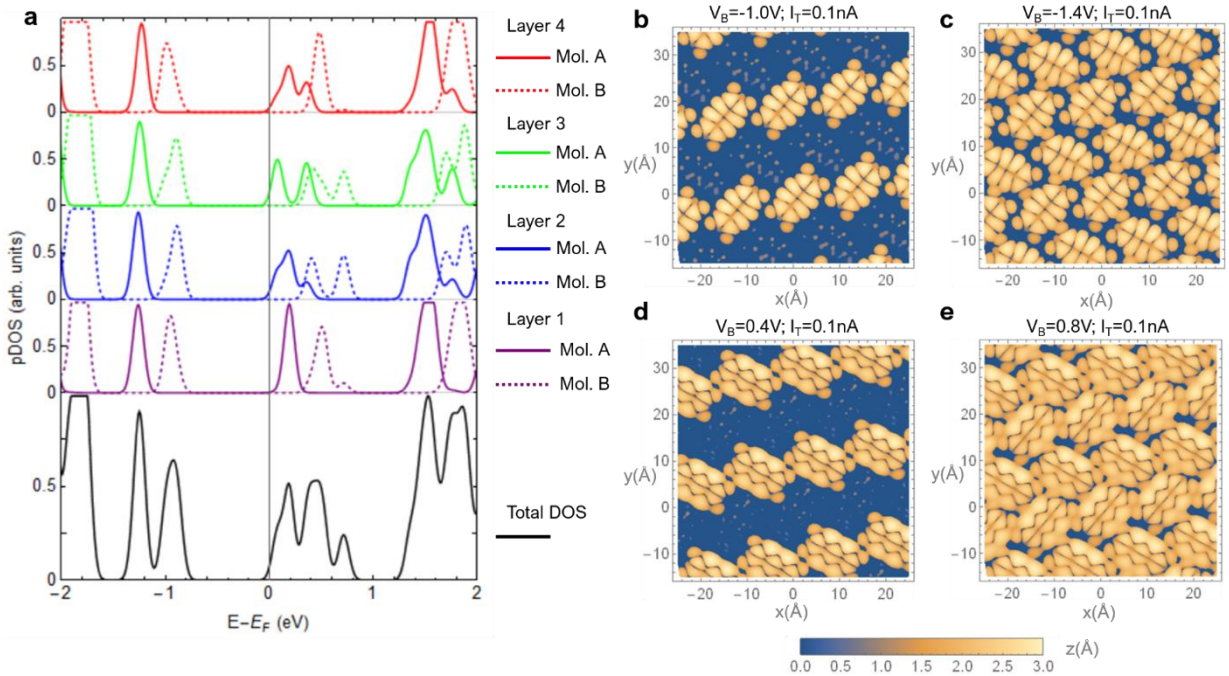

Fig. S15 | 4-Layer PTCDA freestanding. a, Same as Fig. S14 for a self-standing 4-Layer PTCDA slab; in **b-e** the same tunneling parameters as Fig. S14b-e have been used to ease the comparison.

VI. 4 Dipole-transition matrix elements

The DFT calculations give also access to a way to estimate the dipole-transition matrix elements, needed in the two-state model described in section V. Given an initial state, $|i\rangle$, and a final state, $|f\rangle$, the dipole transition matrix element between these states is defined as $\boldsymbol{\mu}_{i,f} = -e\langle i|\boldsymbol{r}|f\rangle$, where e is the elementary charge and $\boldsymbol{r}$ is the position vector. As shown in ref[11], $\boldsymbol{\mu}_{i,f}$ is well defined in the PAW approach used in this work. In Table 3 we report the absolute value of $\boldsymbol{\mu}$ (in atomic units, a.u.) along the three Cartesian directions for an isolated PTCDA molecule and between the HOMO and LUMO states. Only the "x" component has a finite value, whereas the "y" and "z" components vanish due to the D_{2h} symmetry of the molecule, as it can readily be understood if one looks at the shapes of the HOMO and LUMO orbitals shown in Fig. S12b.

Isolated PTCDA

$\|j\rangle$	$\|i\rangle$	ΔE (eV)	$\|\mu_x\|$ (au)	$\|\mu_y\|$ (au)	$\|\mu_z\|$ (au)
HOMO	LUMO	1.47	2.18	8.5×10^{-6}	1.8×10^{-7}

Table 3: Dipole transition matrix elements between HOMO and LUMO of an isolated PTCDA molecule.

Using the results obtained for the monolayer PTCDA on the 15 Layer Au (111) substrate, we can also estimate the dipole transition matrix elements between HOMO and LUMO for this system. The procedure is more cumbersome because, as already observed, it is not possible to assign the HOMO and LUMO orbital of the molecules to a single one electron state, but rather they are shared within groups of states. Hence, to calculate the dipole transition matrix elements, we summed the contributions coming from the different states within each group. If we denote, as in the main text, $\mu_{\parallel}$ the in-plane component and with $\mu_{\perp}$ the out-of-plane one, the absolute value of the dipole matrix elements for the HOMO-LUMO transition obtained taking into consideration the one-electron states with leading HOMO and LUMO character are: $|\mu_{\parallel}| = 1.86$ a.u. and $|\mu_{\perp}| = 0.06$ a.u.. Of course, the "summing" procedure introduces some "error" in the estimate, as it is not possible to disentangle the contribution to the final value of μ coming from the parts of the wavefunction that leak inside the Au slab. Nevertheless, the estimated values are very close to the dipole matrix elements for the isolated molecule, meaning that the introduced error is not very high. Using a

similar procedure, we can also estimate the dipole-transition matrix elements between the HOMO and the gold surface state. Due to the quasi-free electron character of the in-plane wavefunction of the surface state, the "intensity" of μ between the HOMO of PTCDA and the Au (111) surface state depends on the k-point at which μ is calculated. Interestingly enough, $\mu_{\parallel}$ practically vanishes at the Γ point, whereas it has a finite value for $|k_{\parallel}| \neq 0$. This is the consequence of the approximate D_{2h} symmetry of the molecules, in particular of the HOMO shape shown in Fig. S12b, and the fact that, for $|k_{\parallel}| \approx 0$, the Au (111) surface-state wave function barely depends on *x* and *y*. In Fig. S16 we report the absolute value of the in-plane and out-of-plane components of the dipole-transition matrix elements between the HOMO of the PTCDA monolayer and the surface state as a function of the length of the vector $\boldsymbol{k}$ chosen inside the first Brillouin zone (BZ). $\mu_{\perp}$ is almost constant and close to zero for all the investigated k points due to the very limited extension of the HOMO orbital along the *z* direction. On the other hand, $\mu_{\parallel}$ exhibits a linear dependence on the length of the $\boldsymbol{k}$ vector. Assuming that the linear dependence given in Fig. S16 holds for any direction in k-space, we can estimate the mean value of the in-plane dipole-transition matrix element in the first BZ, resulting $\mu_{\parallel}$~0.6 a.u..

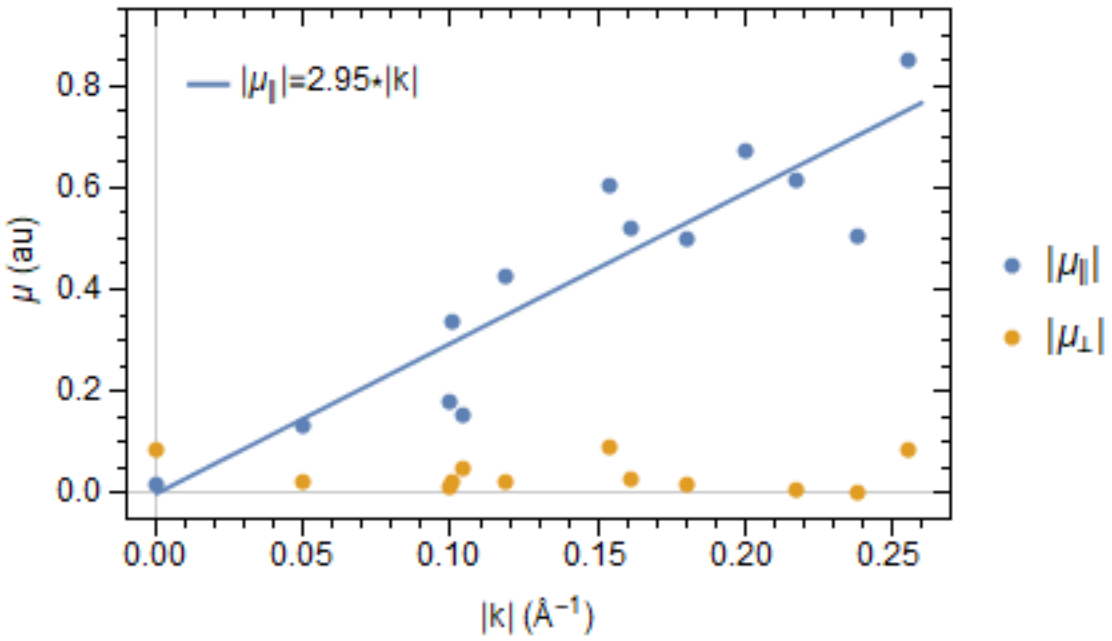

Fig. S16. k-dependence of the dipole-transition matrix elements between the HOMO and surface state for a PTCDA monolayer adsorbed on gold.

Finally, we evaluated the dipole transition matrix elements between the HOMO and LUMO of the 4-layer PTCDA system. Since we have shown above that the gold surface induces only minor changes to the electronic properties of the 4-layer system, we focus our analysis on the free-standing 4-Layer system. As already observed, the "HOMO group" and the "LUMO group" are composed of 8 molecular orbitals. This gives rise to 64 possible HOMO-LUMO transitions per k point. In our calculation we included 7 k points in the first BZ, having a total of 448 HOMO-LUMO combinations. The absolute values of all the in-plane and out-of-plane transition dipole moments are collected in the histograms presented in Fig. S17. As it is clear from this figure, the vast majority of the transition matrix elements (both in the in-plane and in the out-of-plane directions) are zero or very small. This result stems from the fact that, in addition to the above-mentioned symmetry constraints, molecular orbitals localized on different (distant) molecules barely overlap, hence the corresponding μ is small or vanishing. We find several instances in which $\mu_\perp \sim 0.15$ a.u., which is the typical non-vanishing value for $\mu_\perp$. Interestingly, this non-zero value of $\mu_\perp$ is associated with the non-flat geometry of the 4-Layer. Indeed, we verified that, for the perfectly flat geometry, the maximum value of $\mu_\perp$ was less than 0.01 a.u.. From the histograms shown in Fig. S17, we have estimated the mean values of $|\mu_\parallel|$ and $|\mu_\perp|$ by excluding individual transition-dipole matrix elements smaller than 0.1 a.u. (first point of the histograms). The results are $|\mu_\parallel| = 0.83$ a.u. and $|\mu_\perp| = 0.15$ a.u..

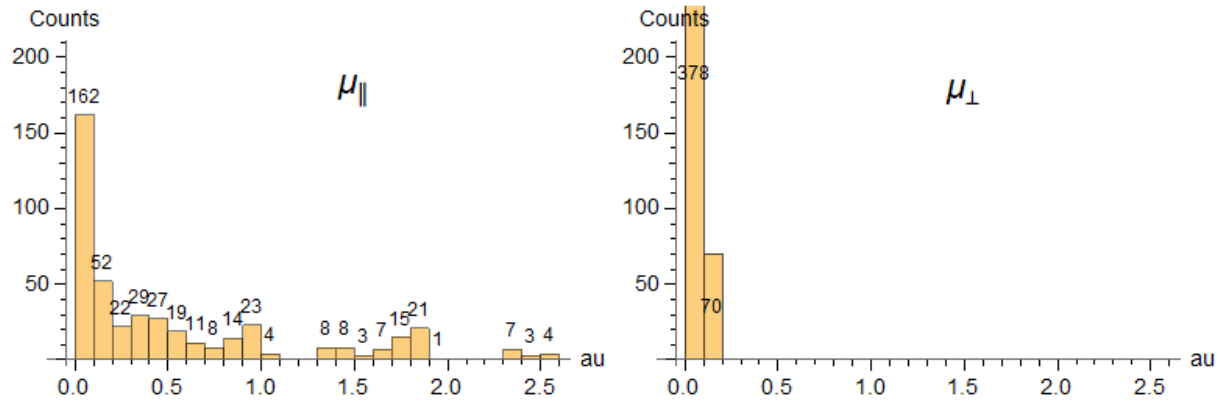

Fig. S17. Histograms of the dipole transition matrix elements (in atomic units, a.u.) for the 4-Layer PTCDA system between the HOMO and the LUMO states for the 7 k-points used in the calculation. The two plots have the same horizontal and vertical scale to ease comparison.

References

1 Blochl, P. E. Projector Augmented-Wave Method. *Phys Rev B* **50**, 17953-17979 (1994).

2 Kresse, G. & Furthmuller, J. Efficiency of ab-initio total energy calculations for metals and semiconductors using a plane-wave basis set. *Comp Mater Sci* **6**, 15-50 (1996).

3 Kresse, G. & Furthmuller, J. Efficient iterative schemes for ab initio total-energy calculations using a plane-wave basis set. *Phys Rev B* **54**, 11169-11186 (1996).

4 Kresse, G. & Joubert, D. From ultrasoft pseudopotentials to the projector augmented-wave method. *Phys Rev B* **59**, 1758-1775 (1999).

5 Perdew, J. P., Burke, K. & Ernzerhof, M. Generalized gradient approximation made simple. *Phys. Rev. Lett.* **77**, 3865-3868 (1996).

6 Tkatchenko, A. & Scheffler, M. Accurate Molecular Van Der Waals Interactions from Ground-State Electron Density and Free-Atom Reference Data. *Phys. Rev. Lett.* **102** (2009).

7 Monkhorst, H. J. & Pack, J. D. Special Points for Brillouin-Zone Integrations. *Phys Rev B* **13**, 5188-5192 (1976).

8 Tersoff, J. & Hamann, D. R. Theory and Application for the Scanning Tunneling Microscope. *Phys. Rev. Lett.* **50**, 1998-2001 (1983).

9 Nicoara, N., Roman, E., Gomez-Rodriguez, J. M., Martin-Gago, J. A. & Mendez, J. Scanning tunneling and photoemission spectroscopies at the PTCDA/Au(111) interface. *Org Electron* **7**, 287-294 (2006).

10 Temirov, R., Soubatch, S., Luican, A. & Tautz, F. S. Free-electron-like dispersion in an organic monolayer film on a metal substrate. *Nature* **444**, 350-353 (2006).

11 Gajdos, M., Hummer, K., Kresse, G., Furthmuller, J. & Bechstedt, F. Linear optical properties in the projector-augmented wave methodology. *Phys Rev B* **73** (2006).